Oceanic Carbon Dioxide Uptake in a Model of Century-Scale Global Warming

Jorge L. Sarmiento; Corinne Le Quere

theoretical percent enrichment for O_3 of isotopic composition (ijk) is given by [RF $({}^{(ijk)}O_3)$/RF$({}^{48}O_3) - 1] \times 100\%$. A particularly significant comparison can be made to the experimental results of Mauersberger *et al.* (8), who measured isotope enrichment for all isotopomers of O_3 using oxygen enriched in ${}^{17}O$ and ${}^{18}O$ (22). The best agreement was achieved for $\beta = 0.78$ (Fig. 1). Using this value for β, RFs of 0.85 and 0.95 were determined for ${}^{48}O_3$ and ${}^{49,50}O_3$, respectively, which compares well with the available experimental results. Uniform agreement with the various laboratory and atmospheric measurements is not expected for at least four reasons. First, the observed isotopic enrichments, and therefore β in this model, vary with experimental conditions. Second, no account was taken of mass-dependent kinetic isotope effects. The importance of this effect is shown by the experimentally observed depletion of ${}^{17}O{}^{17}O{}^{17}O$ and ${}^{18}O{}^{18}O{}^{18}O$ relative to ${}^{16}O{}^{16}O{}^{16}O$ (Fig. 1) in accord with theoretical predictions (23). Third, the possibility of isotopic exchange when M in reaction 3c is O_2 was not considered. Fourth, possible SIKIEs in reactions 3b or 3c were not considered. This last point may be significant because there is some experimental evidence (13, 14) that a decrease in symmetry may enhance the energy transfer stabilization step of the formation mechanism. This effect may be relevant to the enhanced production of ${}^{16}O{}^{16}O{}^{18}O$ relative to ${}^{16}O{}^{18}O{}^{16}O$ observed in some laboratory (24) and atmospheric (25–28) measurements.

Earlier theoretical treatments have attempted to rationalize SIKIEs in O_3 formation in terms of incomplete energy randomization in O_3^* or in terms of excited-state curve crossings (29, 30) but could not account for the special enrichment of the completely asymmetric isotopomer. This enrichment can be rationalized within the conceptual framework presented in this report. The present explanation differs qualitatively from earlier approaches by focusing on the symmetry properties of the infinitely separated $O_2 + O$ reactants and how they correlate with those of O_3^* instead of considering the O_3^* complex only. The interpretation that ${}^{32}O_2(f)$ produces ${}^{48}O_3$ more efficiently than ${}^{32}O_2(e)$ implies by microscopic reversibility that thermal dissociation of ${}^{48}O_3$ will preferentially produce ${}^{32}O_2(f)$ over ${}^{32}O_2(e)$. The experimental investigation of this prediction would provide a stringent test of the theory.

REFERENCES AND NOTES

1. K. Mauersberger, *Geophys. Res. Lett.* **8**, 935 (1981).
2. M. H. Thiemens and J. E. Heidenreich III, *Science* **219**, 1073 (1983).
3. B. Schueler, J. Morton, K. Mauersberger, *Geophys. Res. Lett.* **17**, 1295 (1990).
4. J. Yang and S. Epstein, *Geochim. Cosmochim. Acta* **51**, 2019 (1987).
5. M. H. Thiemens and T. Jackson, *Geophys. Res. Lett.* **15**, 639 (1988).
6. J. Morton, B. Schueler, K. Mauersberger, *Chem. Phys. Lett.* **154**, 143 (1989).
7. M. H. Thiemens and T. Jackson, *Geophys. Res. Lett.* **17**, 717 (1990).
8. K. Mauersberger, J. Morton, B. Schueler, J. Stehr, S. M. Anderson, *ibid.* **20**, 1031 (1993).
9. D. Krankowsky, F. Bartecki, G. G. Klees, K. Mauersberger, K. Schellenbach, *ibid.* **22**, 1713 (1995).
10. G. I. Gellene, in *Advances in Gas Phase Ion Chemistry, vol. 2*, N. G. Adams and L. M. Babcock, Eds. (JAI Press, Greenwich, CT, 1996), pp. 161–191.
11. K. S. Griffith and G. I. Gellene, *J. Chem. Phys.* **96**, 4403 (1992).
12. G. I. Gellene, *ibid.*, p. 4387.
13. _____, *J. Phys. Chem.* **97**, 34 (1993).
14. R. K. Yoo and G. I. Gellene, *J. Chem. Phys.* **102**, 3227 (1995).
15. _____, *ibid.* **105**, 177 (1996).
16. S. Chapman, *Philos. Mag.* **10**, 345 (1930).
17. *L* is the quantum number of the relative orbital angular momentum (**L**) of O_2 and O and M_L is the projection of **L** on a space-fixed *z* axis.
18. Hund's case (a) rotational angular momentum wave functions are labeled by projection of the total electronic orbital angular momentum on the molecule-fixed *z* axis (Λ), the total angular momentum exclusive of nuclear spin (J), the total electron spin angular momentum (S), and the projection of the total electron spin angular momentum on the molecule-fixed *z* axis (Σ). Hund's case (b) nuclear angular momentum wave functions are labeled by the atomic nuclear spin of atoms A and B [$I_a(A)$ and $I_b(B)$, respectively] and the total molecular nuclear spin (I).
19. P. R. Bunker, *Molecular Symmetry and Spectroscopy* (Academic Press, New York, 1979).
20. The operations of $D_{\infty h}(M)$ as applied to the O_2/O supermolecule are the identity, permutation of the atoms in O_2, inversion of all coordinates, and permutation of the atoms in O_2 followed by inversion of all coordinates. They are denoted E, (12), E^*, and (12)*, respectively (Table 1).
21. The statistical *e/f* ratio is determined most simply by considering Hund's case (b) rotational angular momentum wave functions where N, the total angular momentum exclusive of nuclear and electron spin, replaces Σ of Hund's case (a) rotational wave functions. In general, with $S = 1$, there are three values of J ($N - 1$, N, and $N + 1$) for each value of N. Two of these three J levels are e states, and the third is an f state.
22. In contrast to Morton *et al.* (6) and Mauersberger *et al.* (8), J. Yang and S. Epstein [*Geochim. Cosmochim. Acta* **51**, 2011 (1987)] reported no symmetry-dependent isotope effects using O_2 highly enriched in ${}^{17}O$ and ${}^{18}O$. However, it may be significant that Yang and Epstein converted O_3 to O_2 before isotopic analysis, whereas Morton *et al.* and Mauersberger *et al.* isotopically analyzed O_3 directly.
23. J. A. Kaye, *J. Geophys. Res.* **91**, 7865 (1986).
24. S. M. Anderson, J. Morton, K. Mauersberger, *Chem. Phys. Lett.* **156**, 175 (1989).
25. C. P. Rinsland *et al.*, *J. Geophys. Res.* **90**, 10719 (1985).
26. A. Goldman *et al.*, *ibid.* **94**, 8467 (1989).
27. A. Meier and J. Notholt, *Geophys. Res. Lett.* **23**, 551 (1996).
28. F. W. Irion *et al.*, p. 2377.
29. D. R. Bates, *J. Chem. Phys.* **93**, 8739 (1990).
30. J. J. Valentini, *ibid.* **86**, 6757 (1987).
31. This research was supported by the National Science Foundation (CHE95-51008) and the Robert A. Welch Foundation. This material is based in part on work supported by the Texas Advanced Research Program under grant 003644-071.

19 July 1996; accepted 10 October 1996

Oceanic Carbon Dioxide Uptake in a Model of Century-Scale Global Warming

Jorge L. Sarmiento* and Corinne Le Quéré

In a model of ocean-atmosphere interaction that excluded biological processes, the oceanic uptake of atmospheric carbon dioxide (CO_2) was substantially reduced in scenarios involving global warming relative to control scenarios. The primary reason for the reduced uptake was the weakening or collapse of the ocean thermohaline circulation. Such a large reduction in this ocean uptake would have a major impact on the future growth rate of atmospheric CO_2. Model simulations that include a simple representation of biological processes show a potentially large offsetting effect resulting from the downward flux of biogenic carbon. However, the magnitude of the offset is difficult to quantify with present knowledge.

The most important anthropogenic greenhouse gas contributing to increased radiative trapping today and in the foreseeable future is CO_2 (1). International agreements to mitigate increased radiative trapping have begun to take the form of atmospheric CO_2 stabilization scenarios, such as those examined in a recent Intergovernmental Panel on Climate Change (IPCC) study (2–4). The major sinks for anthropogenic CO_2 emis-

sions are the ocean and the terrestrial biosphere. The oceanic sink in the IPCC stabilization scenarios was calculated based on the assumption that the ocean circulation and temperature will remain constant over the next few centuries. However, Manabe and Stouffer (5, 6) have shown that the global warming resulting from increased CO_2 concentrations may have a significant effect on ocean circulation and temperature. Here, we examine the effects of such changes on oceanic CO_2 uptake, using the coupled ocean-atmosphere global warming model of Manabe and Stouffer (5).

Program in Atmospheric and Oceanic Sciences, Princeton University, Princeton, NJ 08544, USA.

*To whom correspondence should be addressed.

The coupled model combines a three-dimensional (3D) atmospheric model and a 3D oceanic general circulation model (GCM) (7). Three climate simulations were carried out (5). The first modeled a "control" climate in which atmospheric CO_2 was kept constant at the initial value of 300 parts per million (ppm). The other two were global warming scenarios in which atmospheric CO_2 was increased at a rate of 1% per year until it had doubled after 70 years ("2 × CO_2" climate change scenario) or quadrupled after 140 years ("4 × CO_2" climate change scenario), after which it was held constant (Fig. 1A). The rate of increase of radiative forcing in these simulations is similar to the "business as usual" scenario of the IPCC (8). We ran our simulations for a total of 350 years.

The most dramatic oceanic responses to the global warming scenarios are the increase in temperature and the reduction in thermohaline circulation (5). Over the 350 years of our simulations, the global mean ocean surface temperature warmed by 2.4°C in the 2 × CO_2 climate change scenario and 4.9°C in the 4 × CO_2 scenario (Fig. 1B). The peak value of the thermohaline circulation in the North Atlantic collapsed from 18.5 Sv (1 Sverdrup = 10^6 m^3 s^{-1}) to about 2.5 Sv in the 4 × CO_2 scenario (Fig.

1C). Other components of the thermohaline circulation, such as the Antarctic Bottom Water circulation, were also reduced (6). The reduced thermohaline circulation in the 4 × CO_2 scenario remains stable over many centuries; the thermohaline circulation in the 2 × CO_2 scenario begins to recover after about 150 years. A weakening or collapse of the global-scale thermohaline overturning as climate warms is a robust result of both 2D (9) and 3D (5) coupled atmosphere-ocean models. The collapse in thermohaline circulation is due primarily to stabilization of the water column by some combination of a poleward shift in mid-latitude precipitation, as in the 3D studies (5), and the impact on the meridional density gradient of greater penetration of the heating anomaly in downwelling regions (9). Manabe and Stouffer (10) have found that the bifurcation to a collapsed circulation that occurs in the 4 × CO_2 scenario depends on the rate of CO_2 increase: At slower increase rates, the thermohaline circulation decreased but did not collapse, even in a 4 × CO_2 scenario.

The first set of ocean CO_2 uptake simulations we describe were performed in a model without ocean biology (11). The pur-

pose of these "solubility model" simulations was to examine the effect of ocean warming and reduced thermohaline circulation unencumbered by the poorly known effects of biology. We carried out two types of solubility model simulations. A first set of baseline simulations was done using the control-climate ocean, but atmospheric CO_2 was fixed at the 2 × CO_2 and 4 × CO_2 curves of Fig. 1A and allowed to invade the ocean. These simulations are equivalent to the IPCC stabilization scenarios in that the ocean circulation remains roughly constant and the temperature does not increase. A second set of simulations combined the 2 × CO_2 and 4 × CO_2 climate change simulations described above with equivalent 2 × CO_2 and 4 × CO_2 ocean, CO_2 uptake simulations.

Annual and cumulative solubility model oceanic CO_2 uptakes (Fig. 2, A and B, and Table 1) show that the baseline solubility model scenarios take up by far the largest amount of CO_2. The reduction in the 350-year cumulative CO_2 uptake in the 2 × CO_2 and 4 × CO_2 climate change scenarios relative to the baseline scenarios is 38 and 49%, respectively (Table 1). The fractional impact on annual uptake in the 4 × CO_2
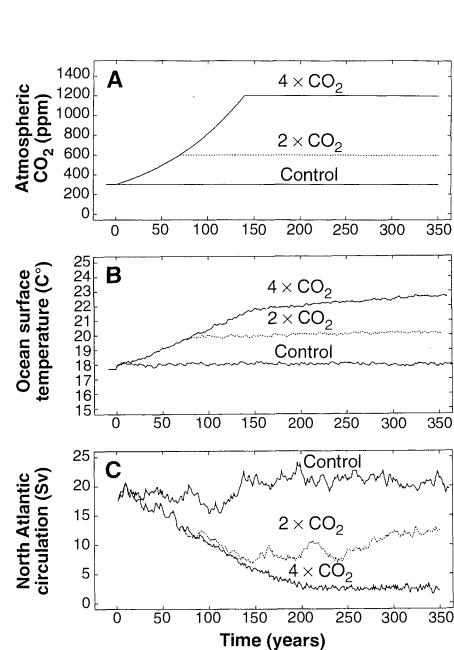
Fig. 1. (A) Atmospheric CO_2 as specified in the control, 2 × CO_2, and 4 × CO_2 model simulations. (B) Global mean ocean surface temperature simulated by the coupled ocean-atmosphere model. (C) Maximum overturning circulation in the North Atlantic thermohaline cell. Note that the North Atlantic thermohaline cell increases slightly in the control scenario over the time span of the simulation. Manabe and Stouffer did not observe such an increase (5), probably because their initial ocean circulation was different from ours.
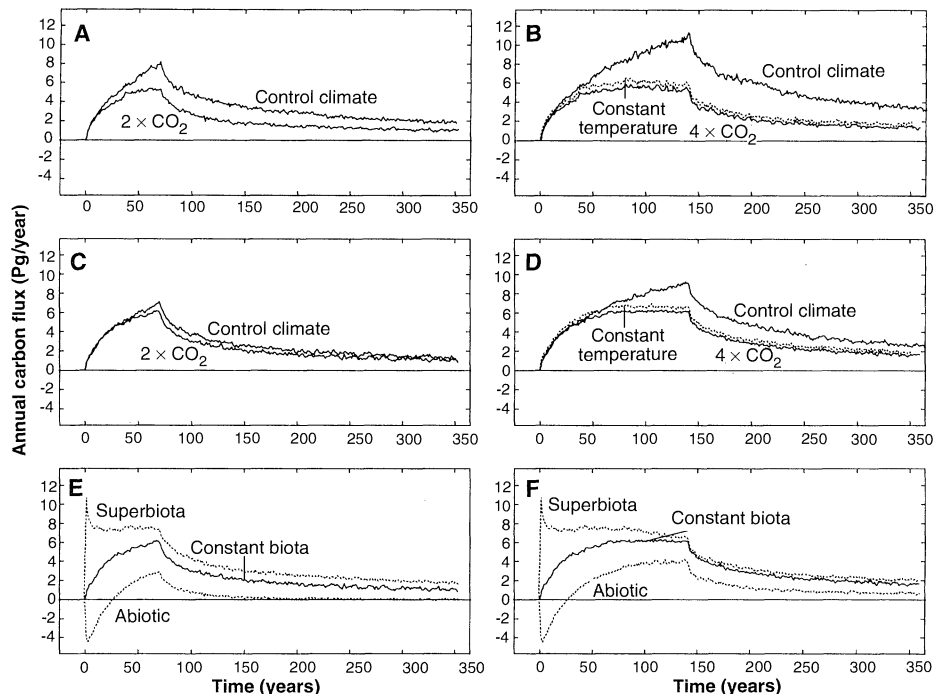
Fig. 2. Annual oceanic uptake of CO_2. (A) The solubility model with atmospheric CO_2 fixed according to the 2 × CO_2 scenario of Fig. 1A. Two scenarios were run: one used the control climate (the baseline scenario) and the other used the 2 × CO_2 climate. (B) The same as (A) but with CO_2 fixed according to the 4 × CO_2 scenario of Fig. 1A. The constant-temperature scenario allows the ocean circulation to change as in the 4 × CO_2 climate but keeps the temperature used for the carbon chemistry calculations fixed at the initial value. (C) and (D) are analogous to (A) and (B), respectively, but were run in the OBM. (E) and (F) show how the oceanic uptake in the OBM changes if the ocean biology is modified to remove all the nutrients at the surface all the time (the superbiota scenario) or if all organisms die (the abiotic scenario).

scenario is greater than about 50% beyond about 150 years (Fig. 2B). We determined the contribution to the temperature increase in the 4 × CO_2 scenario by running a simulation in which the ocean circulation was permitted to change as in the 4 × CO_2 climate change scenario but the ocean temperature used in the carbon chemistry calculations was fixed at the initial seasonally varying steady-state ocean values. The relative contribution of heating is important near the beginning but becomes less so as time goes on (Fig. 2B and Table 1). The final fractional contribution of heating to the difference in uptake between the 4 × CO_2 and control climates is 15%, with the reduced ocean circulation contributing the remaining 85%. Thus, the reduction in uptake is primarily a result of the diminished thermohaline circulation.

In the second set of ocean CO_2 uptake simulations, (i) the biological processes of production of biogenic organic matter, (ii) transport of biogenic material to the deep waters, and (iii) remineralization of biogenic material were included in the model [ocean biogeochemical model (OBM)] (12). The OBM was initialized by running it until the upward flux of remineralized inorganic matter balanced the downward flux of biogenic material. In the absence of a clear understanding of the potential response of biological processes to changes in ocean circulation and temperature, we adopted the simple expedient of assuming that the flux of biogenic material from the surface to the abyss remains constant at its initial estimated magnitude, except in regions where the major nutrient phosphate is depleted at the surface, in which case the production of biogenic material is stopped.

The CO_2 uptake in the constant-biota OBM simulations differed from the solubility model in two respects (Fig. 2, C and D, and Table 2):

1) The ocean takes up less CO_2 in the baseline OBM simulation than it does in the baseline solubility model simulation. The reduction after 350 years is 17% in the 4 × CO_2 simulation and 19% in the 2 × CO_2 simulation. This drop results partly from the combined effect of $CaCO_3$ and nitrate cycling in the OBM. The lower surface alkalinity diminishes the buffering capacity of the ocean and thus its ability to dissolve excess CO_2. The remainder of the reduction in ocean uptake results from the small increase of thermohaline circulation in the control climate simulation (Fig. 1C). The increased ocean circulation augments the upward flux of remineralized carbon in the baseline OBM simulation. Because the downward flux of biogenic material was kept constant, the net effect is to reduce the total oceanic uptake of atmospheric CO_2.

2) The reduction in cumulative 350-year oceanic uptake between the 2 × CO_2 and 4 × CO_2 OBM climate change simulations is 14% [139 petagrams (1 Pg = 10^{15} g) of carbon (Pg C)] and 28% (497 Pg C), respectively. This reduction is much smaller than the values of 38 and 49% obtained in the solubility models. The primary reason that the effect of ocean circulation is smaller in the OBM compared with the solubility model is that the flux of biogenic material to the abyss continues almost unabated, whereas the return flux of inorganic carbon to the surface, which was large enough at the beginning of the simulation to balance the downward flux of biogenic material, is slowed dramatically by the reduction in ocean circulation. Dissolved inorganic carbon formed by the remineralization of biogenic material therefore accumulates at a faster rate in the deep ocean, primarily the thermocline, in the OBM climate change simulations than it does in a model without biology.

Maier-Reimer et al. (13) have also carried out a simulation of the effect of global warming on the uptake of carbon by the ocean. Theirs was an ocean-only model including biology and forced with surface temperatures obtained from a coupled atmosphere-ocean simulation. Their forcing did not include changes in the wind or, more importantly, in mid-latitude precipitation, which Manabe and Stouffer found to be the main cause of the reduction of the thermohaline circulation in their coupled model (5). As a consequence of this and probably other differences in the models, their reduction of 24 to 20 Sv in the North Atlantic thermohaline overturning predicted by the end of the next century was about

Table 1. Cumulative oceanic uptake of anthropogenic CO_2 in the solubility model. The percentage change for the climate change scenarios is the difference from the baseline scenarios. The heating effect was calculated with a simulation that used the ocean circulation from the global warming scenario but fixed the temperature at the initial value before warming. The percentage change is the fractional contribution of heating relative to the total difference between the global warming scenario and control climate.

Year	Oceanic uptake of anthropogenic CO_2 (Pg C)		
	Baseline scenarios	Climate change scenarios	Heating effect
2 × CO_2 (total atmospheric increase at year 70 = 641 Pg C)			
70	362	286 (−21%)	
100	532	390 (−27%)	
200	886	571 (−36%)	
300	1125	700 (−38%)	
350	1223	753 (−38%)	
4 × CO_2 (total atmospheric increase at year 140 = 1911 Pg C)			
100	623	454 (−27%)	52 (31%)
140	1030	670 (−35%)	73 (20%)
200	1476	849 (−42%)	99 (16%)
300	1954	1027 (−48%)	134 (14%)
350	2140	1098 (−49%)	151 (15%)

Table 2. Cumulative oceanic uptake of anthropogenic CO_2 in the OBM. The percentages and details about the heating effect are as in Table 1.

Year	Oceanic uptake of anthropogenic CO_2 (Pg C)				
	Baseline scenarios	Climate change scenarios			Heating effect
	Constant biology	Abiotic	Constant biology	Superbiota	
2 × CO_2 (total atmospheric increase at year 70 = 641 Pg C)					
70	329	25 (−92%)	312 (−5%)	535 (+63%)	
100	469	66 (−86%)	429 (−9%)	692 (+48%)	
200	734	94 (−87%)	644 (−12%)	1005 (+37%)	
300	908	103 (−89%)	781 (−14%)	1230 (+36%)	
350	978	105 (−89%)	839 (−14%)	1324 (+35%)	
4 × CO_2 (total atmospheric increase at year 140 = 1911 Pg C)					
100	554	130 (−77%)	496 (−10%)	756 (+36%)	48 (84%)
140	899	286 (−68%)	742 (−17%)	1027 (+14%)	67 (43%)
200	1257	400 (−68%)	964 (−23%)	1270 (+1%)	90 (31%)
300	1631	492 (−70%)	1190 (−27%)	1534 (−6%)	122 (28%)
350	1774	527 (−70%)	1277 (−28%)	1642 (−7%)	138 (28%)

half the reduction from 19 to 10 Sv that we obtained in the comparable 100-year result of our $4 \times CO_2$ OBM simulation. However, the effect of the global warming scenario in reducing oceanic CO_2 uptake is similar in both models: 42 Pg C in (13) versus 58 Pg C in ours (Table 2). This likeness occurs because in the $4 \times CO_2$ OBM, most of the effect of reduced thermohaline circulation is canceled by the downward flux of biogenic material during the first century. The dominant process contributing to the reduction in CO_2 uptake is thus the increase in ocean temperature (84%) (Table 2). Without biology, as in the solubility model, warming contributes only 31% of the reduced oceanic CO_2 uptake (Table 1).

The slower ocean circulation in the constant-biology $2 \times CO_2$ and $4 \times CO_2$ climate change simulations relative to the control causes an imbalance in which the downward flux of biogenic material is no longer in equilibrium with the upward flux of inorganic carbon formed by remineralization of the biogenic material. There is an imbalance because the constant-biology model assumes that the flux of biogenic material remains unchanged except where phosphate runs out at the surface. We examined the sensitivity of the oceanic CO_2 uptake to the biological processes by determining (i) an upper limit from a "superbiota" simulation in which the biology was assumed to respond to climate change by increasing its efficiency to the point of eliminating surface phosphate everywhere, and (ii) a lower limit from an "abiotic" simulation in which all organisms died so that there was no production of biogenic material or remineralization of dissolved organic carbon. The ocean biology was modified instantaneously at the beginning of the simulation. Such rapid changes in ocean biology are, of course, unrealistic; thus, the impacts calculated for the early years of the simulation are greatly exaggerated, and even the final results should be considered extreme limits, because neither is likely to be achieved.

Simulations were performed for the upper limit superbiota scenario and the lower limit abiotic scenario in the $2 \times CO_2$ and $4 \times CO_2$ climates (Fig. 2, E and F, and Table 2). The final cumulative uptake in the $2 \times CO_2$ scenario ranges from 105 to 1324 Pg C, and in the $4 \times CO_2$ simulations, from 527 to 1642 Pg C. The difference between the upper and lower limits, 1219 Pg C in the $2 \times CO_2$ scenario and 1115 Pg C in the $4 \times CO_2$ scenario, is much greater than would have been expected on the basis of box and other ocean model simulations of the pre–Industrial Revolution ocean that do not include the large increase in anthropogenic CO_2 (4,

14). In the latter models, the full range between abiotic and superbiotic scenarios is about 600 Pg C after equilibrium has been reached, which takes several thousand years. The greater response of the $2 \times CO_2$ and $4 \times CO_2$ increase scenarios is attributable to the large reduction in the ocean CO_2 buffering capacity in scenarios such as these, as previously noted in connection with the IPCC scenarios (3). The decrease in ocean buffering capacity results from the reaction of CO_2 molecules with carbonate ions and water to form bicarbonate ions. As this reaction proceeds, the carbonate ion concentration is reduced and the buffering capacity diminishes. Thus, the ocean buffering capacity is much smaller in the $4 \times CO_2$ scenario than it is in the $2 \times CO_2$ scenario and is much smaller in both of these compared to a scenario without anthropogenic CO_2. The comparable range of the $2 \times CO_2$ and $4 \times CO_2$ simulations at 350 years is probably a transient effect attributable to the fact that ocean circulation is greater in the $2 \times CO_2$ scenario than it is in the $4 \times CO_2$ scenario.

The overall results of the biology sensitivity studies indicate that an improved knowledge of ocean biology is necessary if we are to estimate what the oceanic uptake would be for climate change scenarios such as those studied here. The uncertainty in cumulative 350-year ocean uptake that results from our ignorance of biological processes is certainly a few hundred, possibly as much as 1000, petagrams of carbon.

Analysis of the models described here show that most of the oceanic CO_2 uptake occurs in the Southern Ocean (Table 3). The Southern Ocean is also the region that has by far the largest impact on the response of oceanic CO_2 uptake to global warming (Table 3). Most of the reduction in CO_2 uptake in the solubility model relative to its baseline occurs in the Southern Ocean. The greatest difference between the solubility model and OBM is in the Southern Ocean. The greatest sensitivity to the superbiota and abiotic simulations is in the Southern Ocean, which

agrees with previous sensitivity studies using a steady-state ocean (15). Other regions sensitive to the biology include, in order of decreasing importance, the North Atlantic, the North Pacific, and the equatorial band (15). There is, as yet, no consensus in the oceanographic community as to what controls the efficiency of organic matter formation in these regions, although many theories exist (16). Focused research—such as the ongoing international Joint Global Ocean Flux Study and efforts to develop a long-term monitoring capability through satellite observations of ocean color—is needed in order to improve our understanding of oceanic biological processes.

An area of particular importance is our understanding of the processes that led to the reduced atmospheric CO_2 content of the last ice age (17) because similar processes may be involved in future responses to global warming. An important conclusion of our study is that the magnitude of future atmospheric CO_2 responses to such changes would be greatly magnified because of the reduced buffering capacity of the ocean under increased atmospheric CO_2. This observation may also be relevant to periods in the distant past when atmospheric CO_2 appears to have been much higher than at present (18).

The total anthropogenic CO_2 emissions that would be permitted in the $2 \times CO_2$ and $4 \times CO_2$ climate change scenarios are the sum of the specified atmospheric increase plus the oceanic uptake. This calculation ignores the possible contribution of terrestrial processes, which may be quite large (2). Over the 350-year period of our integration, the atmospheric increase in the $2 \times CO_2$ atmospheric increase and climate change scenario is 641 Pg C, and the oceanic uptake in the constant biology simulation is 839 Pg C (131% of the atmospheric increase). The equivalent numbers in the $4 \times CO_2$ scenario are 1911 Pg C in the atmosphere and 1277 Pg C in the ocean (67% of the atmospheric increase). The contribution of the oceanic sink is substantially smaller

Table 3. Latitudinal breakdown of the 350-year cumulative atmosphere-ocean flux of anthropogenic CO_2 in the $4 \times CO_2$ scenario. The column labeled "Reduction" refers to the change relative to the baseline value; the "Increase" column refers to the change in reduction.

Region	Flux of anthropogenic CO_2 (Pg C)			
	Baseline solubility model	Reduction due to climate change	Increase due to biology	Superbiota minus abiotic
North of 30°N	382	−257	61	159
30°S to 30°N	493	−41	−76	273
South of 30°S	1265	−744	193	683

than it would be if the ocean circulation remained constant (-139 Pg C in 2 $\times$ CO_2 simulation and -497 Pg C in the 4 $\times$ CO_2 simulation), and it has an uncertainty of plus or minus several hundred petagrams because of our limited understanding of the biological response.

REFERENCES AND NOTES

1. K. P. Shine, Y. Fouquart, V. Ramaswamy, S. Solomon, J. Srinivasan, in *Climate Change 1994*, J. T. Houghton *et al.*, Eds. (Cambridge Univ. Press, Cambridge, 1995), pp. 161–203.
2. I. G. Enting, T. M. L. Wigley, M. Heimann, *Assessment of the IPCC CO_2 Modelling Study* (Division of Atmospheric Research, Commonwealth Scientific and Industrial Research Organisation, Aspendale, Victoria, Australia, 1994).
3. J. L. Sarmiento, C. Le Quéré, S. W. Pacala, *Global Biogeochem. Cycles* **9**, 121 (1995).
4. D. Schimel *et al.*, in (*1*), pp. 35–71.
5. S. Manabe and R. J. Stouffer, *Nature* **364**, 215 (1993).
6. _____, *J. Clim.* **7**, 5 (1994).
7. The atmospheric and oceanic models have a latitudinal spacing of 4.5°, and the longitudinal spacing is 3.75° in the oceanic model and 7.5° in the atmospheric model. The ocean has 12 vertical levels, and the atmosphere has nine. Simple models of sea ice and terrestrial heat and water budgets are also incorporated. The two GCMs were initialized independently using seasonal solar insolation and observed ocean surface temperature and salinity to force them until a steady-state was achieved. We minimized the drift that occurs upon coupling the models by adjusting the fluxes of heat and water by an amount that varied with region and season but remained constant throughout the global warming scenarios [S. Manabe, R. J. Stouffer, M. J. Spelman, K. Bryan, *J. Clim.* **4**, 785 (1991)].
8. J. T. Houghton, G. J. Jenkins, J. J. Ephraums, Eds., *Climate Change, The IPCC Scientific Assessment* (Cambridge Univ. Press, New York, 1990).
9. L. D. D. Harvey, *J. Geophys. Res.* **99**, 18447 (1994).
10. S. Manabe and R. Stouffer, personal communication.
11. All solubility model simulations were carried out using the full coupled ocean-atmosphere model. The carbon chemistry was modeled using previously described techniques (*19*). The air-sea flux of CO_2 was calculated using a wind-speed–dependent gas exchange coefficient [R. Wanninkhof, *J. Geophys. Res.* **97**, 7373 (1992)] multiplied by the air-sea CO_2 difference. The partial pressure of CO_2 in the atmosphere (pCO_2) was specified according to the curves in Fig. 1A. We calculated the surface ocean pCO_2 by solving the full carbon chemistry equations, which required specification of the temperature, salinity, alkalinity, and total carbon content of the ocean. The temperature and salinity were obtained from the models. The alkalinity was modeled in the same way as salinity, with the global mean alkalinity initialized to the observed value. The initial total carbon distribution for the CO_2 uptake simulations was obtained in an ocean-only model by fixing atmospheric pCO_2 at 300 ppm and allowing it to invade the ocean until the ocean was in equilibrium with the atmosphere, that is, the global air-sea flux was zero.
12. The initial condition for the OBM was obtained with the use of an ocean-only model. Formation of organic matter in the surface ocean was determined by forcing the seasonal model surface phosphate toward the observed annual mean phosphate distribution (seasonal data coverage is poor) with a 100-day time scale. Organic carbon formation was calculated using an organic matter C:P ratio of 120. Half of the organic matter formed at the surface was put into particulate matter that is exported to the deep ocean and remineralized instantaneously, following a scaling obtained from sediment-trap

observations [J. H. Martin, G. A. Knauer, D. M. Karl, W. W. Broenkow, *Deep-Sea Res.* **34**, 267 (1987)]. The other half was put into a semilabile dissolved organic carbon pool that decays to inorganic carbon with a mean life of 11.3 years, obtained by requiring that the total semilabile dissolved organic carbon pool remained fixed at its observed value (*19*). The cycling of $CaCO_3$ was calculated by forcing the horizontally averaged alkalinity profile toward the observed values, after first normalizing both the model and observations to a constant salinity and correcting them for the effect of nitrate cycling. The resulting fits of the model to the annual mean nutrient, carbon, and alkalinity data are very good, and the model has a realistic regional distribution of annual mean air-sea fluxes. The 100-day forcing time scale used to predict surface production of organic matter permits seasonal fluctuations to occur. However, because we used annual mean phosphate observations to determine the new production, the seasonal phosphate and CO_2 fluctuations do not agree very well with seasonal observations in the few regions where such data are available.
13. E. Maier-Reimer, U. Mikolajewicz, A. Winguth, *Clim. Dyn.* **12**, 711 (1996).
14. J. L. Sarmiento and J. R. Toggweiler, *Nature* **308**, 621 (1984).
15. J. L. Sarmiento and J. C. Orr, *Limnol. Oceanogr.* **36**, 1928 (1991).
16. S. W. Chisholm and F. M. M. Morel, Eds., *ibid.*, pp. 1507–1965.
17. A. Neftel, H. Oeschger, J. Schwander, B. Stauffer, R. Zumbrunn, *Nature* **295**, 220 (1982); D. Raynaud *et al.*, *Science* **259**, 926 (1993).
18. R. A. Berner, *Am. J. Sci.* **294**, 56 (1994).
19. J. L. Sarmiento, R. Murnane, C. Le Quéré, *Philos. Trans. R. Soc. London* **348**, 211 (1995).
20. We thank R. Stouffer for assisting us in implementing the coupled model, and both him and S. Manabe for their enthusiastic support and comments on the manuscript. The carbon cycle model was developed by R. Murnane, and both he and R. Slater provided important help interpreting the results. R. Toggweiler, D. Baker, and D. Harvey provided helpful comments on the manuscript. T. Hughes helped analyze the results. We thank J. Mahlman for his comments and the support that the NOAA Geophysical Fluid Dynamics Laboratory has provided for our research over a period of many years through the ocean group headed by R. Toggweiler. Additional support was provided by grants from the NOAA Office of Global Programs, the National Science Foundation, and the Department of Energy.

Red-Emitting Semiconductor Quantum Dot Lasers

S. Fafard,* K. Hinzer, S. Raymond, M. Dion, J. McCaffrey, Y. Feng, S. Charbonneau

Visible-stimulated emission in a semiconductor quantum dot (QD) laser structure has been demonstrated. Red-emitting, self-assembled QDs of highly strained InAlAs have been grown by molecular beam epitaxy on a GaAs substrate. Carriers injected electrically from the doped regions of a separate confinement heterostructure thermalized efficiently into the zero-dimensional QD states, and stimulated emission at ~707 nanometers was observed at 77 kelvin with a threshold current of 175 milliamperes for a 60-micrometer by 400-micrometer broad area laser. An external efficiency of ~8.5 percent at low temperature and a peak power greater than 200 milliwatts demonstrate the good size distribution and high gain in these high-quality QDs.

Semiconductor quantum well laser diodes based on two-dimensional density of states are technologically important because of their high power, high efficiency, and wide tunability (*1*). Recently, a breakthrough in nano-optics research has permitted the direct growth of semiconductor QDs (*2, 3*). These QDs have discrete zero-dimensional (0D) energy levels and can be thought of as artificial atoms (*4–16*). In much the way water vapor condenses into droplets on a piece of glass, in the Stranski-Krastanow growth mode during the molecular beam epitaxy (MBE) of highly strained material, small defect-free islands of uniform size form. If a low band gap semiconductor is embedded in higher band gap material, quantum confinement in all three directions results. This spon-

taneous island formation has been exploited to produce self-assembled QDs with a variety of III-V semiconductors.

For most materials studied, emission from self-assembled QDs is in the infrared (IR), but radiative recombination in the red part of the visible spectrum has also been achieved (*4, 10*). These high-quality nanostructures feature a variety of interesting properties such as extremely sharp homogeneous linewidths (*4, 5, 7, 10, 14*), invariant lifetimes and linewidths for temperatures up to the onset of the thermionic emission (*14*) state-filling and excited-state emission (*6, 8, 12, 13, 16*), and distinctive carrier dynamics and phonon interactions (*8, 15*). Moreover, the one-step in situ fabrication process of these self-assembled QDs makes them technologically compatible with current device structures.

Theory predicts that QD laser structures should have higher gain, lower

Institute for Microstructural Sciences, National Research Council of Canada, Ottawa, Ontario, Canada K1A 0R6.

*To whom correspondence should be addressed.